Fe3+-doped ordered mesoporous γ-Fe2O3/SiO2 microspheres as a highly efficient magnetically separable heterogeneous Fenton catalyst

Nassira Ferroudj, Patricia Beaunier, Anne Davidson, Sébastien Abramson

Microporous and Mesoporous Materials xxx (xxxx) 111373

Contents lists available at ScienceDirect

Microporous and Mesoporous Materials

journal homepage: www.elsevier.com/locate/micromeso

Fe^{3+}-doped ordered mesoporous γ-Fe_2O_3/SiO_2 microspheres as a highly efficient magnetically separable heterogeneous Fenton catalyst

Nassira Ferroudj [a, b], Patricia Beaunier [c], Anne Davidson [c], Sébastien Abramson [a, *]

[a] Laboratoire de PHysico-chimie des Electrolytes et Nanosystèmes InterfaciauX (PHENIX UMR 8234, Sorbonne Université- CNRS), Sorbonne Université, 4, place Jussieu, 75252, Paris, France

[b] Laboratoire de Génie Chimique et Environnement de Skikda (LGCES), Université 20 Août 1955 Skikda, BP 26 Route d'El Hadaiek, Skikda, Algeria

[c] Laboratoire de Réactivité de Surface (LRS UMR 7197, Sorbonne Université- CNRS), Sorbonne Université, 4, place Jussieu, 75252, Paris, France

ARTICLE INFO

Keywords:
Ordered mesoporous materials
Magnetic nanocomposites
Iron oxide nanoparticles
Silica
Heterogenous fenton catalyst
Methyl orange
Reactive black 5

ABSTRACT

Here, several γ-Fe_2O_3/SiO_2 nanocomposite microspheres were synthesized, characterized and tested as magnetically separable heterogeneous catalysts in an advanced oxidation process. A strong relation between the structure and the activity of these materials was evidenced. Two parameters, including the porosity of the silica support and the doping of the material with Fe^{3+} ions in addition to the γ-Fe_2O_3 nanoparticles, were investigated. The structure of the catalytic materials was determined by the use of different methods, in particular SEM, TEM, XRD, N_2 physisorption, magnetometry, UV–Vis spectroscopy and XPS. The results demonstrated that the irregular microporosity of the silica framework can be replaced by an ordered mesoporosity, adding a second surfactant during the synthesis. For the mesoporous material, it was observed that the additional Fe^{3+} are dispersed in the mesoporous silica framework as individual cations and small clusters of Fe(III) species. The materials were tested as heterogeneous Fenton catalysts on two model aqueous pollutants, methyl orange (MO) and reactive black 5 (RB5). It was observed that the oxidation and mineralization rates of the two dyes is significantly enhanced when a doped catalytic material is used. This effect is particularly strong with the mesoporous silica support. In addition, the doped mesoporous catalyst retained its activity for a large range of conditions. These improvements were attributed to the strong activity of the additional Fe(III) species, although the presence of the mesoporosity also plays a significant role.

1. Introduction

The replacement of homogenous catalysts by their heterogeneous counterparts is a major issue in different areas of chemistry, including chemical engineering, organic synthesis, materials science, and environmental technologies. The main motive for these efforts is that heterogeneous catalysts can be easily recovered, recycled and reused, which can decrease the environmental and economical costs of the chemical processes. However, heterogeneous catalysts frequently suffer from relatively poor catalytic activity due to slow external and internal diffusion rates, or to limited phase transfers onto the solid surface [1]. This drawback can be avoided by using finely divided catalytic nanomaterials, although their activity can be sometimes restricted by their aggregation during the course of the reaction, and their recovery can be complex when they are dispersed in a liquid phase [2]. The deposition of the nanocatalyst onto a support may overcome these problems, which requires a good control over the support size and porosity and catalyst dispersion. It must also be checked whether the chemical composition of the catalytic surface is modified or not by the presence of the support [2,3]. This implies a thorough characterization of the nanocomposite catalyst, with the final goal of optimizing its properties.

These considerations are especially true for heterogeneous Fenton catalysts, which are applied for the decontamination of aqueous effluents. The Fenton-type reactions belong to the vast class of advanced oxidation processes (AOPs), which have in common to allow the generation of the hydroxyl ($HO^{\bullet}$) radicals. These species are characterized by a high reductive potential (E^0 = 2.8 V vs. SHE) and are therefore able to react with numerous organic molecules, allowing their oxidation and in some ideal instances their complete mineralization [4]. This is a promising way for the treatment of toxic organic micropollutants which cannot be removed by the usual treatment methods. For the conventional Fenton processes, the $HO^{\bullet}$ radicals are formed from H_2O_2 and a homogenous catalyst, usually the Fe^{2+} or Fe^{3+} ions [5]. However, a large number of works have been carried out to replace the soluble ions

* Corresponding author.
E-mail address: sebastien.abramson@sorbonne-universite.fr (S. Abramson).

https://doi.org/10.1016/j.micromeso.2021.111373
Received 7 June 2021; Received in revised form 23 July 2021; Accepted 15 August 2021
1387-1811/

by a heterogeneous catalyst with two main objectives: to facilitate the recycling of the catalyst, and to allow the use of a neutral pH, since homogeneous catalyst are limited to a narrow pH range, generally around 3 [6]. Typical heterogeneous catalysts include Fe^{2+}/Fe^{3+} exchanged zeolites or clays, and iron oxide phases, which can be dispersed onto various supports such as silicas, aluminas, polymers or carbons [6–11]. The possible beneficial effect of the support on the catalytic activity has been attested by several studies, since a better dispersion of the catalyst and a larger adsorption of the pollutants can be obtained when a support is added [12–16]. However, supported catalysts may also suffer from low activities, and sometimes from problems of leaching related to the dissolution of iron [17–20]. To improve the catalytic performance, two complementary strategies can be employed. First, the diffusion of the reactants and products can be improved by increasing the size, volume, and regularity of the pores inside the support [21–23]. Secondly, the number and the efficiency of the catalytic sites can be increased by playing on the dispersion and composition of the active phase. To this aim, the iron-based nanocomposite catalyst can be doped by a second metal which can be dispersed under the form of isolated ions (Fe^{3+}, Al^{3+}, Cu^{2+} …) [24–26], metal oxide phase (MnO_2, Al_2O_3, CuO, Cu_2O, Mn_3O_4 …) [15,27–31], or noble metal nanoparticles (Pt, Au …) [32,33]. Various mechanisms have been proposed to explain the increased activities obtained with the doped catalysts. Among others, the presence of the second phase could provide additional catalytic sites [24,32], may favor the dispersion of the iron oxide particles on the support [27], increase the electron densities on the active sites improving the adsorption and degradation rate of H_2O_2 [25,26], or accelerate the regeneration step of the catalytic species [15,31]. Such explanations seem to strongly depend on the nature of the support and the metal species.

In our previous studies, we employed maghemite (γ-Fe_2O_3) nanoparticles (NPs) supported on microporous silica microspheres as heterogeneous Fenton catalysts [20,34,35]. The main advantage of this material is to be easily recoverable with the help of a simple magnet, as a result of the high magnetic susceptibility of the γ-Fe_2O_3 NPs. We also observed a low level of leaching and a good reusability for this catalyst, but relatively low activities, and moderate mineralization levels, were obtained in the absence of light [20,35]. However, we reported that the efficiency of this material can be improved through the use of visible light [34]. But photoactivation is not always practicable at a large scale, or when the effluent is characterized by a high level of turbidity or absorbance [36]. The aim of the present work is to demonstrate how the catalytic activity of the maghemite/silica nanocomposite microspheres (γ-Fe_2O_3/SiO_2 MS) can be considerably improved in dark Fenton processes thanks to a fine control of their structure, without major loss of their recoverability and stability. Two parameters have been especially changed. First, the microporous porosity of the silica support has been replaced by a regular mesoporosity. Secondly, the catalyst has been doped by addition of Fe^{3+} ions during the synthesis, along with the presence of the γ-Fe_2O_3 NPs. Thus, four maghemite/silica nanocomposite catalysts have been studied here. The first catalyst is constituted by the undoped microporous microspheres (γ-Fe_2O_3/SiO_2 MS). They were obtained by a previously reported Emulsion Solvent Evaporation (ESE) method [20], based on the gelification of sol droplets containing a silica precursor and the γ-Fe_2O_3 NPs in a vegetable oil. The synthesis of the three other catalysts is based on the same strategy, although small modifications were introduced to disperse extra-Fe^{3+} ions inside the silica matrix, and/or to create an ordered mesoporosity.

To highlight the catalysts structure-activity relationships, we decided to study the Fenton oxidation and mineralization of two model dyes, methyl orange (MO) and reactive black 5 (RB5). The pollution of water effluents by dyes is a major concern, especially in regions where textile industry is developed [7]. RB5 and MO were chosen because of their moderate adsorption on the catalysts [20], and for their relative structural proximity (see Fig. S1). Nevertheless, the two dyes can be distinguished by their size: RB5 is a much larger molecule than MO, which is helpful to understand how the catalytic properties are affected by the steric constraints. The effect of a Fe^{3+} doping on magnetically separable iron oxide/mesoporous silica was already studied by Xia et al. [24]. Here, the objective is to explore the effect of mesoporosity and Fe^{3+} doping both in combination and separately, in order to determine the role played by each parameter on the structure of the material and on the catalytic activity. Therefore, the catalytic materials were thoroughly characterized through the use of different methods, to establish with a high accuracy the structure of the catalysts, and how it contribute to the improvement of the activity.

2. Experimental part

2.1. Catalysts preparation

2.1.1. Preparation of the maghemite nanoparticles (γ-Fe_2O_3 NPs)

The γ-Fe_2O_3 NPs used in this study were the same as those used in our previous papers [20,34,35]. The first step is the coprecipitation of Fe^{2+} and Fe^{3+} ions in order to get magnetite (Fe_3O_4) NPs [37]. To this end, a mixture of 715 mL of iron chloride (III) ($FeCl_3$ at 2,2 mol L^{-1}) and 180 g of iron chloride (II) ($FeCl_2$) was added to 100 mL of aqueous hydrogen chloride (HCl at 37%). Then, 1 L of aqueous ammonia (NH_3 at 20%) was rapidly added to this mixture.

This suspension was vigorously stirred during 30 min and, afterwards, placed over a magnet. The supernatant was removed, and the NPs were washed with 1L of distilled water. Hence, 2 L of aqueous nitric acid (HNO_3) at 2 mol L^{-1} (prepared from a commercial HNO_3 solution at 52%) was added, and the suspension was stirred for 30 min. Finally, the supernatant was removed using a magnet, and the black mixture, typical of Fe_3O_4 NPs, was obtained.

The second step is the oxidation of Fe_3O_4 by iron nitrate to produce the γ-Fe_2O_3 NPs [20,38]. To do so, 323 g of iron (III) nitrate nonahydrate ($Fe(NO_3)_3.9H_2O$) was added to the Fe_3O_4 NPs aqueous suspension and this new mixture was left stirring at 100 °C for 30 min. A change of color was observed from black to deep brown indicating the formation of the γ-Fe_2O_3 NPs. After sedimentation and removal of the supernatant, 360 mL of nitric acid (HNO_3 at 52%) and 2 L of distilled water were added, and the suspension was stirred during 10 min. Finally, the NPs were successively washed three times with acetone, two times with diethyl ether, before to be redispersed by addition of 1 L of distilled water. . The γ-Fe_2O_3 NPs were thus obtained as a stable aqueous acidic dispersion, also called ferrofluid.

2.1.2. Preparation of the maghemite/silica microspheres

The *undoped maghemite/silica microporous microspheres* (γ-Fe_2O_3/SiO_2 MS) were synthesized using a modified ESE (emulsion solvent evaporation) protocol [39] described in our previous papers [20,34,35]. Briefly, a silica precursor (tetraethoxysilane, TEOS, 20 mL) was hydrolyzed by stirring during 45 min with a 0.15 mol L^{-1} HNO_3 aqueous solution (5 mL). Then, 50 mL of a magnetic sol was obtained by adding to this mixture the γ-Fe_2O_3 NPs dispersion (25 mL, diluted in a 10^{-2} mol L^{-1} HNO_3 aqueous solution, at a NPs concentration equivalent to 0.25 mol L^{-1} of Fe). 40 mL of this sol was added dropwise to an organic phase (360 mL) composed of a vegetable oil (usually commercial rapeseed oil from Lesieur) and a commercial emulsifier (0.1% w/w of Arlacel P135 from Uniquema), under stirring. This water-in-oil emulsion was transferred into a Buchner flask, and the ethanol formed by the TEOS hydrolysis was evaporated during 45 min at 35 °C under reduced pressure, which led to the rapid condensation of the silica in each water droplet. The emulsion was stirred overnight at atmospheric pressure, before to be broken by addition of a large amount of acetone. The silica microspheres containing the γ-Fe_2O_3 NPs were washed several times with acetone and water, and dried at 70 °C. Finally, the beads were cal-

cined in an oven under air at 400 °C for 18 h to remove any organic traces.

The synthesis of heterogeneous Fenton-type catalysts by dispersion of metallic ions inside the core of porous silica particles has been largely reported [7,8,15,21,24–28,40]. Two main methods have been developed. The ions can be co-condensed with the silica precursor [21,24–26,28,40], or the silica support can be first synthesized, and hence impregnated by a solution containing the ions [15,27,40]. However, it has been found that the impregnation method leads to less stable catalysts [40]. We chose then to introduce the Fe^{3+} ions by a co-condensation method. Therefore, the *Fe^{3+}-doped maghemite/silica microporous microspheres* (Fe/γ-Fe_2O_3/SiO_2 MS), were prepared using the same procedure as for the γ-Fe_2O_3/SiO_2 MS, except that 1 g of iron (III) nitrate nonahydrate ($Fe(NO_3)_3.9H_2O$) was also added to the initial magnetic sol.

The addition of an ordered mesoporosity into a silica framework can be easily performed by adding a surfactant capable of forming a lyotropic liquid crystal. The polymerization of silica takes place around the ordered micelles formed by the surfactant. Two major types of ordered mesoporous silicas, frequently abbreviated as MCM-41 and SBA-15 materials, are available depending on the composition of the surfactant [41,42]. Here, we focused our attention on the synthesis of SBA-15 silicas, since it has been demonstrated that these supports are less sensitive to water [43]. Therefore, the *undoped maghemite/silica ordered mesoporous microspheres* (γ-Fe_2O_3/SiO_2 *m*-MS) were obtained by adding large amount of a hydrophilic surfactant, Pluronic P123, to the sol. In addition, the silica condensation was made at a much more acidic pH, which has been found to favor the development of a well-ordered network of cylindrical mesopores, with sizes between 8 and 12 nm [42,44]. The overall procedure is as follows. To prepare the initial magnetic sol, 6 g of the commercial triblock copolymer, Pluronic P123 (average molecular weight $M_n \approx 5800$ g mol^{-1}, purchased from Aldrich), was added to the γ-Fe_2O_3 NPs dispersion (25 mL), TEOS (20 mL), and a strongly acidic 2 mol L^{-1} HNO_3 aqueous solution (5 mL). After addition of the magnetic sol (40 mL) to the organic phase (360 mL), more drastic conditions were used to evaporate the ethanol formed by the TEOS hydrolysis: the emulsion was transferred into Buchner flask and stirred at 40 °C during 90 min under reduced pressure. The resultant mixture was stirred again at atmospheric pressure overnight, and the emulsion was broken by addition of acetone. Hence, the microspheres were washed several times with acetone and water, before to be dried at 70 °C. Finally, the remaining organic matter (surfactants and traces of oil) were removed from the beads by calcination in air at 400 °C for 18 h.

The *Fe^{3+}-doped maghemite/silica ordered mesoporous microspheres* (Fe/γ-Fe_2O_3/SiO_2 *m*-MS) catalyst were similarly obtained, by combining the addition of iron (III) nitrate nonahydrate ($Fe(NO_3)_3.9H_2O$) with the introduction of Pluronic P123 and condensation at very acidic pH. They were synthesized following the same procedure as for the γ-Fe_2O_3/SiO_2 *m*-MS, except that 1 g of iron (III) nitrate nonahydrate ($Fe(NO_3)_3.9H_2O$) was also added to the initial magnetic sol.

2.2. Characterization methods

The morphology of the MS catalysts was investigated using field emission scanning electron microscope (SEM) on a SEM-FEG Hitachi SU-70 apparatus. The images were taken in secondary electron mode with an accelerating voltage of 10 kV. Prior to analysis, the beads were coated with a thin shell of gold by sputter deposition. Low-magnification Transmission electron microscopy (TEM) measurements were carried out on a JEOL 100CX UHR transmission electron microscope at an acceleration voltage of 100 kV. High-magnification TEM coupled with the selected area electron diffraction (SAED) and energy dispersive X-ray spectroscopy (EDXS) techniques was also performed on a JEOL JEM 2011 transmission electron microscope at an acceleration voltage of 200 kV equipped with a selected energy-dispersive X-ray spectroscopy microanalyzer PGT-IMIX PC. Before TEM analyses, the samples were embedded in a resin (AGAR 100), which was then polymerized at 60 °C during 2 days, and cut in 70 nm thin sections using a LEICA ULTRACUT UCT microtome apparatus.

The textural characteristics of the samples, specific surface area, pore volumes and diameters, were evaluated on a ASAP 2020 Micromeretics apparatus by Nitrogen adsorption/desorption isotherms at −196 °C. Prior to analysis, the samples were degassed overnight at 110 °C under high vacuum (10^{-6} bar). The specific surface area was determined using the multipoint BET method. The pore size distribution was obtained following the Barret-Joyner-Halender method. The pore volume was measured from the nitrogen adsorption volume at a P/P_0 value corresponding to the end of the adsorption step related to the filling of the pores.

Powder X-ray diffraction (XRD) patterns at large and small angles were recorded on a Bruker D8 diffractometer using a Bragg-Brentano geometry and the Cu K_α wavelength ($\lambda = 1.5418$ Å) as X-ray source. The data were collected in the 2θ range from 1° to 4° with a step of 0.02° for small angle analysis, and in the 2θ range from 10° to 70° with a step of 0.039° for large angle analysis, respectively.

The magnetic properties of the materials were studied with a SQUID magnetometer (Quantum Design MPM-5S apparatus) at 25 °C. The samples were analyzed in powdered form. The magnetization–demagnetization curves, M = f(H), where H is the external magnetic field (in Oe), and M the magnetization of the sample (in emu g^{-1}), were normalized to 1 g of γ-Fe_2O_3.

The UV–visible–NIR spectra measurements of the samples were carried out with a diffuse reflectance cell (internal sphere) in the range 200–2500 nm on a Varian Cary 400 spectrometer. Teflon powder was used as a blank.

The chemical state of the surface elements was measured by X-ray photoeletron spectroscopy (XPS) with an Scienta Omicron Argus photoelectron spectrometer using a monochromatized Al K_α radiation source ($h\nu = 1486.6$ eV) having a beam power of 300 W. The powder samples were prepared for measurements by pressing them on an indium foil. Before analysis, the samples were outgassed at room temperature to a pressure of 1×10^{-6} Pa. The area of the analyzed samples was approximatively 1 mm^2. The emission of photoelectrons from the sample was analyzed at a takeoff angle of 45° under ultra-high vacuum conditions (1×10^{-8} Pa). The high resolution XPS spectra of the C_{1s}, O_{1s}, Fe_{2p} and Si_{2p} were collected at a pass energy of 20 eV, and the binding energies were calibrated to the C_{1s} peak at 284.8 eV. To determine the contribution of the different states, the spectra were subtracted by a Shirley background, and fitted with components obtained by a product of Gaussian and Lorentzian functions in a 70–30 ratio.

The iron content in the catalysts was determined by chemical analysis (see Table S1 for the detailed composition of the four catalysts). Prior to analysis, a given weight of material was introduced in a 4 mol L^{-1} HCl aqueous solution. After 48 h of stirring, the γ-Fe_2O_3 NPs were totally dissolved. The iron concentration in the supernatant was then analyzed by atomic absorption spectrophotometry (PerkinElmer AA100 apparatus), allowing the calculation of the Fe_2O_3 weight fraction in the catalysts, w_{Fe2O3}. The values found for w_{Fe2O3} ranges between 7 and 8% for the undoped materials, and 10–12% for the Fe^{3+} doped materials. The larger values obtained for the doped materials is related to the presence of additional Fe(III) species in the silica framework originating from the iron (III) nitrate added during the synthesis. For the doped materials, we evaluated that the fraction of additional Fe(III) species with respect to the total iron is 20% and 40%, respectively for the microporous (Fe/γ-Fe_2O_3/SiO_2 MS) and ordered mesoporous (Fe/γ-Fe_2O_3/SiO_2 *m*-MS) samples.

2.3. Catalytic degradation experiments

The efficiency of the prepared materials as heterogeneous Fenton catalyst was investigated by studying the degradation of two model aqueous dyes, methyl orange (MO) and reactive black 5 (RB5). The structure of these compounds can be found in Fig. S1 of the electronic supplementary information. All the tests were carried out in the dark at a mild temperature (T = 40 °C), in a closed vessel to avoid evaporation. In the usual experiments, the following conditions were used. First, a given mass of catalyst, equivalent to a total iron concentration in the reaction mixture of $[Fe]_T = 3.15 \times 10^{-2}$ mol L^{-1} (the total iron is the sum of the Fe^{3+} ions contained in the γ-Fe_2O_3 NPs and those resulting from the addition of $Fe(NO_3)_3.9H_2O$), was added to a 10^{-3} mol L^{-1} HNO_3 aqueous solution (the volume of the aqueous solution was 8,86 mL for MO, and 8,91 mL for RB5). The exact mass for the catalyst ranged between 0.30 and 0.35 g for the undoped materials, and 0.21–0.25 g for the Fe^{3+}-doped materials, depending on the value of w_{Fe2O3}. Then, a given volume of a mother aqueous solution of $5,44 \times 10^{-3}$ mol L^{-1} of MO, or $6,09 \times 10^{-3}$ mol L^{-1} of RB5, was added to the suspension of the catalyst. The added volume of the pollutant mother solution was 0.46 mL for MO or 0.41 mL for RB5, in such a way that the initial concentration of the pollutant in the final mixture (after addition of H_2O_2) was $C_i = 2.5 \times 10^{-4}$ mol L^{-1} for a total volume of 10 mL. The suspension containing the catalyst and the pollutant was magnetically stirred for 2 h to reach the adsorption equilibrium. Then, to initiate the degradation reaction, 0.68 mL of a 30% w/w H_2O_2 aqueous solution was added to the suspension (corresponding to an initial concentration of H_2O_2 of 0.68 mol L^{-1} in the final mixture). The decolorization kinetic of the solution was followed by the following procedure. Solution samples were taken (typically 150 μL) at desired time intervals, and were put over a magnet to separate the supernatant from the catalysts by magnetically assisted sedimentation. The supernatant was then recovered and diluted to an adequate concentration before to be studied with an UV–Visible spectrophotometer (UVIKON XL apparatus). The remaining concentration of the pollutant in the supernatant (C_t) was determined using the Beer-Lambert law at 502 and 599 nm respectively for MO, and RB5. The initial time t = 0 was fixed at the moment of adding H_2O_2. The concentration of the pollutant in the supernatant measured at t = 0 was noted C_0. C_0 varied between 1.2 and 1.6×10^{-4} mol L^{-1} for MO (35–50% of MO initially adsorbed on the catalysts) and between 1.9 and 2.4×10^{-4} mol L^{-1} for RB5 (5–25% of RB5 initially adsorbed on the catalysts). A slightly larger level of adsorption for the dyes was usually obtained with the ordered mesoporous catalysts.

The initial rate of decolorization (v_0) was determined by plotting the tangent at t = 0 of the kinetic curve $C_t = f(t)$. The decolorization yield (*DY*) at 2 h, was also evaluated from this curve, using the following formula

$$DY = 100\text{-}100 \cdot C_{2h}/C_0$$

Where C_{2h} and C_0 are the concentrations of pollutant in the supernatant respectively at t = 0 and 2 h.

The removal of the total organic carbon (TOC) was determined by a similar procedure analyzing the Non-Purgeable Organic Carbon (NPOC) in the supernatant using a Shimadzu TOC ASI-5000A apparatus. The mineralization yield at 4 h (*MY*) was calculated with the formula

$$MY = 100\text{-}100 \cdot NPOC_{4h}/NPOC_i$$

Where $NPOC_{4h}$ is the NPOC concentration in the supernatant at t = 4 h, and $NPOC_i$, the initial NPOC concentration in the supernatant before the adsorption equilibrium (both are given in ppm).

The iron leaching was determined by measuring the iron concentrations in the supernatant at 4 h using atomic absorption spectrophotometry. The percentage of iron leached (*FeL*) was calculated with the formula

$$FeL = 100 \cdot [Fe]_{s,4h}/[Fe]_T$$

Where $[Fe]_{s,4h}$ is the iron concentration in the supernatant at 4 h, and $[Fe]_T$ the total equivalent iron concentration used in the catalytic test ($[Fe]_T = 3.15 \times 10^{-2}$ mol L^{-1}).

The effect of pH, H_2O_2 initial concentration ($[H_2O_2]_0$), and initial amount of catalyst on the performance of the γ-Fe_2O_3/SiO_2 MS and Fe/γ-Fe_2O_3/SiO_2 *m*-MS materials was studied on the MO degradation. As regards pH, the HNO_3 solution was replaced by pure water and NaOH solution, respectively for pH 5 and 8. Three $[H_2O_2]_0$ values, corresponding to 0.68, 0.068 and 0.0068 mol L^{-1} were tested, by adjusting the added volume of 30% w/w H_2O_2 aqueous solution (0.68, 0.068 and 0.0068 mL, respectively). The amount of catalyst was studied by changing the initial mass. For the γ-Fe_2O_3/SiO_2 MS sample, five values were tested, with initial masses ranging from 0.05 to 0.35 g ($[Fe]_T = 5.1 \times 10^{-3}$ to 3.70×10^{-2} mol L^{-1}), while for the Fe/γ-Fe_2O_3/SiO_2 *m*-MS sample four values ranging from 0.01 to 0.21 g ($[Fe]_T = 1.6 \times 10^{-3}$ to 3.15×10^{-2} mol L^{-1}) were used. The reuse of the catalysts for four times was tested using MO as model pollutant. The reuse tests were performed as follow. After each catalytic test (corresponding to 4 h of reaction), the catalyst was separated from the solution by magnetic settlement, rinsed two times with 10^{-3} mol L^{-1} HNO_3 aqueous solution, and two times with water to remove any possible contaminant from the surface. The solid was finally dried in an oven at 70 °C overnight before the next use. To take into account the catalyst lost after each cycle, while keeping the catalyst, pollutant and H_2O_2 concentrations constant, the volumes of HNO_3, MO and H_2O_2 solutions were adjusted for each reuse test.

For each of these studies, all the parameters were kept constant as in the usual procedure (except that one which was varied). It should be noted, however, that for the highly active Fe/γ-Fe_2O_3/SiO_2 *m*-MS catalyst, a lower mass of 0.03 g ($[Fe]_T = 5,3 \times 10^{-3}$ mol L^{-1}) was used for the studies on $[H_2O_2]_0$ effect and reuse tests.

3. Results and discussion

3.1. Characterization of the catalytic materials

The four catalysts were first characterized by electronic microscopy. The SEM images of each material can be found in Fig. 1.

As can be seen by the SEM images, for each sample, the particles are polydisperse, with diameters ranging from 500 nm to 10 μm. However, the addition of $Fe(NO_3)_3$ and/or Pluronic P123 significantly impacts the morphology of the particles. This is clearly observed by the SEM images. For the microporous samples, the Fe/γ-Fe_2O_3/SiO_2 MS display a less smooth and more faceted external surface (Fig. 1, B) than the γ-Fe_2O_3/SiO_2 MS obtained by the standard synthesis (Fig. 1, A). Concerning the ordered mesoporous materials (γ-Fe_2O_3/SiO_2 *m*-MS and Fe/γ-Fe_2O_3/SiO_2 *m*-MS), both exhibit an irregular faceted shape with the presence of holes on their surface (Fig. 1C and D). Additionally, the images clearly point to the presence of an important void in the particles centre. This suggests that the presence of a second surfactant have a strong effect on the properties of the emulsion during the synthesis of the particles.

The internal structure of the particles was examined by TEM. Several images at different magnifications are presented in Fig. 2. The internal framework of the microspheres seems to be poorly modified by the Fe^{3+} doping, since the two microporous materials (γ-Fe_2O_3/SiO_2 and Fe/γ-Fe_2O_3/SiO_2 MS) appears identical. Both samples are characterized by a homogenous dispersion of the γ-Fe_2O_3 NPs inside the silica matrix (see Fig. 2A and B and C). Regarding the materials prepared with a second surfactant (γ-Fe_2O_3/SiO_2 *m*-MS and Fe/γ-Fe_2O_3/SiO_2 *m*-MS), the TEM images prove that a regular mesoporosity has been effec-

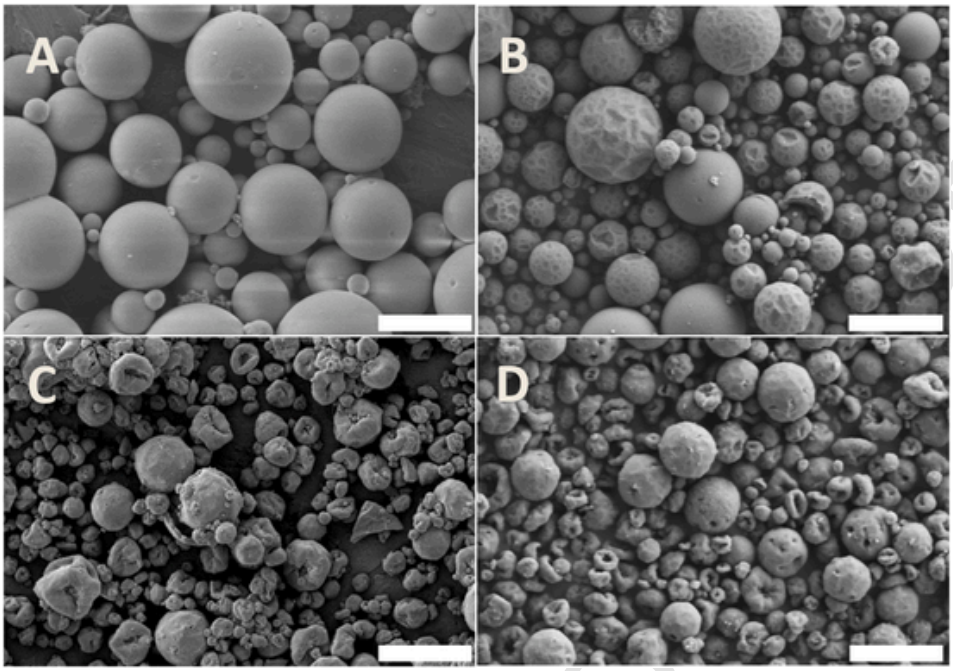

Fig. 1. SEM images of the catalytic materials: (A): γ-Fe_2O_3/SiO_2 MS; (B): Fe/γ-Fe_2O_3/SiO_2 MS; (C): γ-Fe_2O_3/SiO_2 *m*-MS; (D): Fe/γ-Fe_2O_3/SiO_2 *m*-MS. The scale bare is 10 μm.

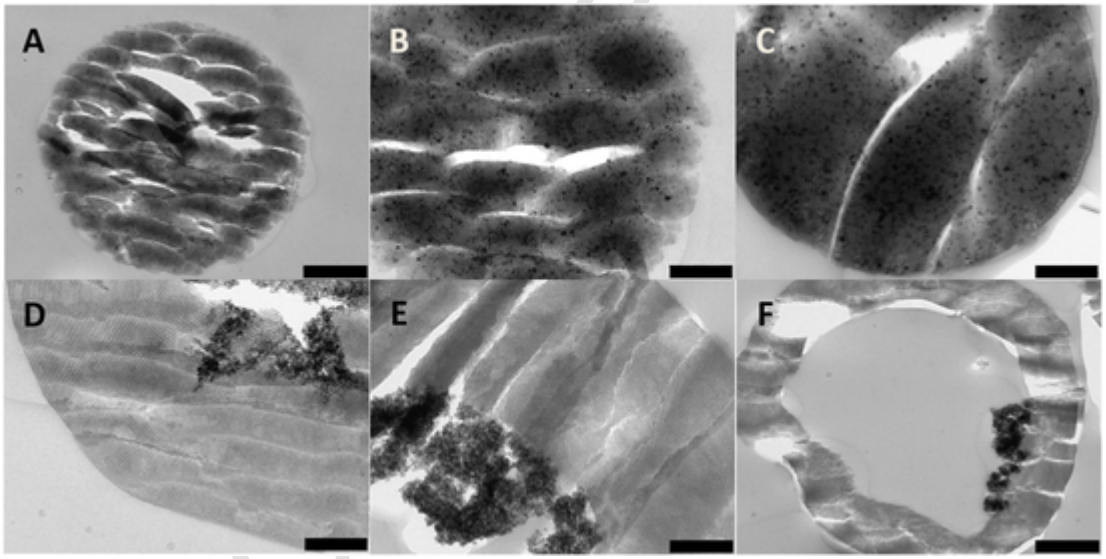

Fig. 2. TEM images of the catalytic materials: (A) and (B): γ-Fe_2O_3/SiO_2 MS; (C): Fe/γ-Fe_2O_3/SiO_2 MS; (D): γ-Fe_2O_3/SiO_2 *m*-MS; (E) and (F): Fe/γ-Fe_2O_3/SiO_2 *m*-MS. For (A) and (F), the scale bar is 500 nm (magnification × 8000). For (B), (C), (D) and (E), the scale bar is 200 nm (magnification × 20000).

tively introduced inside the particles (see Fig. 2D and E and F). These sample exhibit an organised network of parallel mesopores having a cylindrical shape and a constant diameter of few nanometers. The presence of the organised mesoporosity is explained by the polymerization of the silica around the micelles of pluronic P 123 inside the sol droplets, in accordance with previous studies on SBA-15 materials [42,44]. Two additional characteristics are observed for the mesoporous particles. First, a separation has occurred between the silica and the γ-Fe_2O_3 NPs, resulting in the aggregation of the NPs inside the cores of the microspheres. This phenomenon may be explained by the strong acidic pH used during the synthesis, which does not favor the dispersion of the NPs. Secondly, the TEM confirms the hollow morphology of the particles. The image of Fig. 2, F spectacularly illustrates this characteristic (see also Fig. S2 in ESI). This behavior is explained by the modification of the emulsion properties during the synthesis, because of the addition of the second surfactant. Some observations by optical microscopy have suggested that an oil-in water-in oil double emulsion is formed, leading to

the polymerization of the silica around the internal oil droplets, which are finally converted into internal cavities.

The two ordered mesoporous materials were additionally characterized by high-magnification TEM coupled with the SAED and EDXS techniques (see Fig. 3 and Fig. S3). Two major findings were obtained. First, it was confirmed that the aggregated NPs near the centre of the silica particles are effectively the γ-Fe_2O_3 NPs added in the synthesis solution. For the two materials, a SAED pattern was obtained from the diffracted electrons when the beam was focused on the aggregated NPs (see Fig. 3A and B, for the Fe/γ-Fe_2O_3/SiO_2 *m*-MS sample and fig. S3, A and B, for the γ-Fe_2O_3/SiO_2 *m*-MS sample).. On the SAED image, six main diffraction rings corresponding to reticular distances of 2.96, 2.54, 2.04, 1.70,

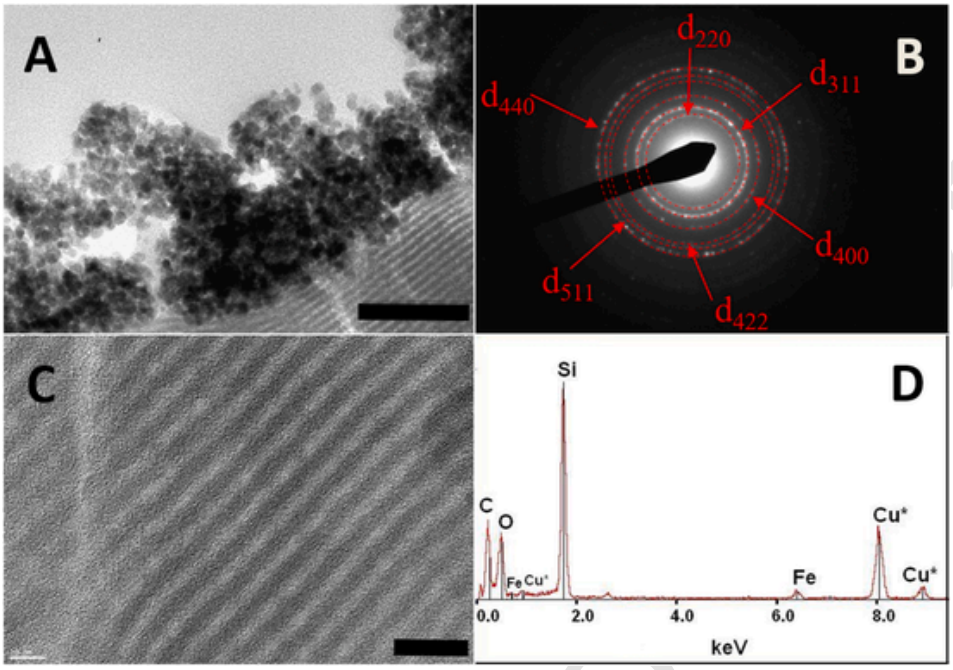

Fig. 3. High-magnification TEM/SAED/EDXS characterization of the Fe/γ-Fe_2O_3/SiO_2 *m*-MS material. (A): TEM image, and (B): corresponding SAED pattern, for the region related to the aggregated γ-Fe_2O_3 NPs (the red rings correspond to the main d_{hkl} lattice fringes). (C): TEM image, and (D): corresponding EDX spectrum, for the region related to the mesoporous silica network. For (A) and (C), the scale bars are respectively 100 and 20 nm (magnifications × 60000 and × 200000). * = The Cu peaks are due to the copper grid. (For interpretation of the references to color in this figure legend, the reader is referred to the Web version of this article.)

1.64 and 1.50 Å were observed and associated respectively to the d_{220}, d_{311}, d_{400}, d_{422}, d_{511}, and d_{440} distances of the γ-Fe_2O_3 structure (ICDD PDF Card No. 39–1346). Secondly, we controlled if iron species were dispersed in the silica framework for the materials synthesized with $Fe(NO_3)_3$. The EDX spectrum corresponding to the mesoporous silica for the Fe/γ-Fe_2O_3/SiO_2 *m*-MS material shows the presence of a small peak at 6.4 keV attributed to the K_α line of iron (see Fig. 3C and D). This peak is not found for the γ-Fe_2O_3/SiO_2 *m*-MS material (see fig. S3, C and D). Thus, at least a part of the iron species due to the $Fe(NO_3)_3$ has been introduced inside the silica network. In this region, no diffraction is observed, which eliminates the presence of crystalline iron oxide. This stands for the presence of isolated ions or small clusters of iron oxide.

To have a more accurate idea of the porosity, N_2 physisorption measurements and low-angle XRD were carried out. The N_2 adsorption-desorption isotherms (see Fig. 4, A and Table S2) confirm the regular mesoporosity of the materials synthesized with the second surfactant. The isotherms corresponding to the γ-Fe_2O_3/SiO_2 *m*-MS and Fe/γ-Fe_2O_3/SiO_2 *m*-MS materials are

of type IV. They display a strong adsorption step with a typical hysteresis, which corresponds to the filling of the mesopores. The relative sharpness of the adsorption step indicates that the mesoporosity is regular. The mean pores diameter calculated by the BJH methods is 3.5 nm, in good agreement with the estimates from TEM images. On the contrary, the isotherms corresponding to the γ-Fe_2O_3/SiO_2 MS and Fe/γ-Fe_2O_3/SiO_2 MS materials are of type I, which is characteristic of microporous solids. The mesoporous volumes for the γ-Fe_2O_3/SiO_2 *m*-MS and Fe/γ-Fe_2O_3/SiO_2 *m*-MS materials are respectively 0.40 and 0.37 $cm^3\ g^{-1}$. These values are

larger than the microporous volumes obtained for the γ-Fe_2O_3/SiO_2 MS and Fe/γ-Fe_2O_3/SiO_2 MS samples (0.25 $cm^3\ g^{-1}$ and 0.23 $cm^3\ g^{-1}$, respectively). Large BET surface areas were therefore calculated for the mesoporous solids, ranging between 565 $m^2\ g^{-1}$ and 608 $m^2\ g^{-1}$, respectively for the Fe/γ-Fe_2O_3/SiO_2 *m*-MS and γ-Fe_2O_3/SiO_2 *m*-MS materials. The two other solids are also characterized by large surface areas, due to the importance of their micropores (according to the BET equation, the values for the γ-Fe_2O_3/SiO_2 MS and Fe/γ-Fe_2O_3/SiO_2 MS materials are 578 $m^2\ g^{-1}$ and 510 $m^2\ g^{-1}$). It should be noted that the addition of the iron (III) nitrate salt has a poor influence on the porosity. The two mesoporous solids were additionally examined by low-angle powder XRD (Fig. 4, B). Both diffractograms exhibit a single sharp peak at $2\theta = 1.3°$, resulting from the existence of a regular spacing between the mesopores. The value of the spacing obtained from the Bragg law is ap-

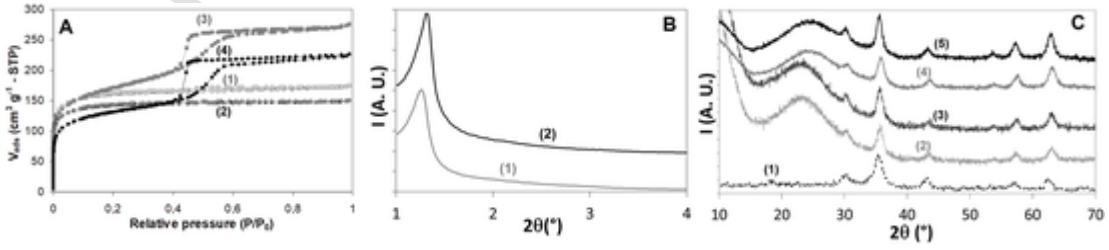

Fig. 4. Characterization of the catalysts by N_2 physisorption and XRD. (A): N_2 adsorption-desorption isotherms. (1): γ-Fe_2O_3/SiO_2 MS; (2): Fe/γ-Fe_2O_3/SiO_2 MS; (3): γ-Fe_2O_3/SiO_2 *m*-MS; (4): Fe/γ-Fe_2O_3/SiO_2 *m*-MS. (B): Small angle XRD patterns for the two mesoporous catalysts. (1): γ-Fe_2O_3/SiO_2 *m*-MS; (2): Fe/γ-Fe_2O_3/SiO_2 *m*-MS. (C) Large angle XRD patterns. (1): bare γ-Fe_2O_3 NPs; (2): γ-Fe_2O_3/SiO_2 MS; (3): Fe/γ-Fe_2O_3/SiO_2 MS; (4): γ-Fe_2O_3/SiO_2 *m*-MS; (5): Fe/γ-Fe_2O_3/SiO_2 *m*-MS.

proximatively 6.8 nm. This is relatively large, when comparing with the mean pore diameter of 3.5 nm, that may be explained by the existence of relatively thick silica walls surrounding the mesopores. The lack of other diffraction peaks at low angle dismisses the existence of a single crystal structure formed by the mesopores.

At larger values of 2θ, XRD was useful to study the crystal structure of the iron oxides. The $10° < 2\theta < 70°$ diffractograms of the four catalytic materials can be found in Fig. 4, C. For comparison, the XRD of the bare γ-Fe_2O_3 NPs was also added. The diffractograms are very similar, all of them exhibiting the characteristic peaks of the main *d*-spacings of the maghemite crystal structure, with comparable widths, as a result of the embedding of the γ-Fe_2O_3 NPs in silica. For the two doped materials, the absence of another crystalline phase resulting from the addition of the $Fe(NO_3)_3$ is supported by the lack of additional peak. The large band between 15° and 30° observed for all the supported materials is related to the presence of the amorphous silica.

To identify the nature of the poorly crystalline iron species resulting from the addition of $Fe(NO_3)_3$, the materials were characterized by several additional methods. The magnetization-demagnetization curves, determined using a vibrating sample magnetometer and normalized to 1 g of maghemite, can be found in Fig. 5, A. All the curves are nearly superimposable and are typical of a superparamagnetic behavior, as a result of the encapsulation of the γ-Fe_2O_3 NPs inside silica. However, small differences can be highlighted by a thorough examination of the curve slopes at high field (see the inset of Fig. 5, A). While the magnetization of the

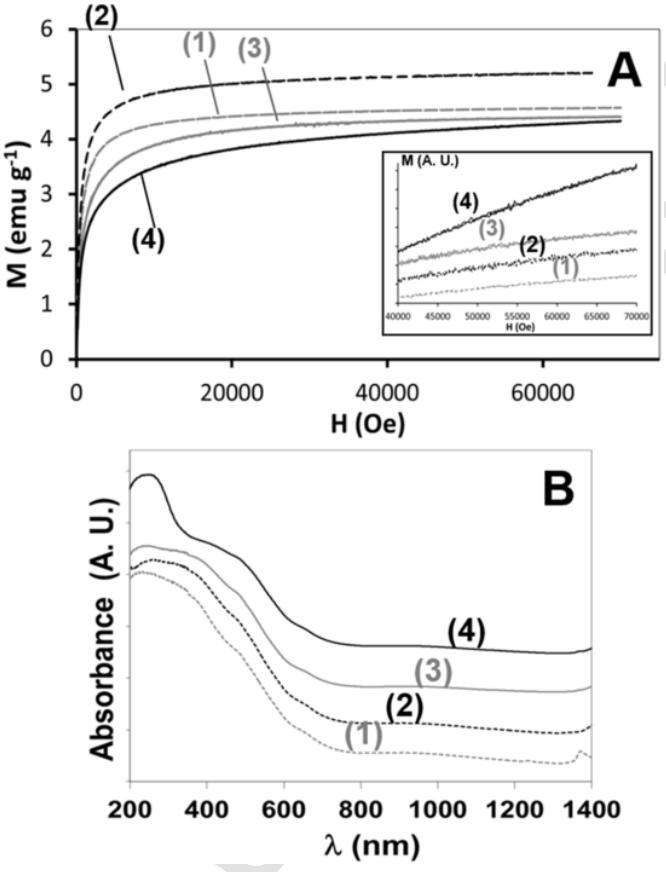

Fig. 5. (A): Magnetization-demagnetization curves of the samples. (1): γ-Fe_2O_3/SiO_2 MS; (2): Fe/γ-Fe_2O_3/SiO_2 MS; (3): γ-Fe_2O_3/SiO_2 *m*-MS; (4): Fe/γ-Fe_2O_3/SiO_2 *m*-MS. The magnetization value, M (in emu g^{-1}), is normalized to 1 g of γ-Fe_2O_3. In inset: Magnetization curves at high field (the curves were intentionally translated to highlight their difference in slope at high field). (B): Diffuse reflectance UV–Vis–NIR spectra of the catalysts. (1): γ-Fe_2O_3/SiO_2 MS; (2): Fe/γ-Fe_2O_3/SiO_2 MS; (3): γ-Fe_2O_3/SiO_2 *m*-MS; (4): Fe/γ-Fe_2O_3/SiO_2 *m*-MS.

undoped materials is nearly constant, because the saturation magnetization of the maghemite is reached, the magnetizations of the doped materials, especially that of the mesoporous sample, slightly increases. This results from the presence of some paramagnetic species originating from the addition of $Fe(NO_3)_3$. The diffuse reflectance UV–Visible–NIR spectra of the samples is shown in Fig. 5, B. All the spectra are characterized by a large absorption band at $\lambda \leq 600$ nm. This band is mainly due to O^{2-}/Fe^{3+} charge transfer transitions, enhanced at higher wavelengths (400–700 nm) by magnetic coupling between the Fe^{3+} cations and crystal field "d-d" transitions [45]. The spectra of the two undoped samples are identical because the two solids contain only the γ-Fe_2O_3 NPs. The spectrum of the doped microporous solid is also nearly-identical to the spectra of these two samples, which may indicate that the absorption of the iron species resulting from the $Fe(NO_3)_3$ is screened by the absorption of the γ-Fe_2O_3 NPs. In contrast, the spectrum of the mesoporous doped sample exhibits a sharp absorption band between 200 and 350 nm with a maximum at $\lambda = 245$ nm, which is superimposed to the absorption band of the γ-Fe_2O_3 NPs. This additional absorption band corresponds to Fe^{3+} isolated cations, or to small iron oxide clusters, both resulting from the addition of $Fe(NO_3)_3$. A more accurate attribution can be made regarding the previous works on the UV–Vis spectra of Fe-exchanged ZSM-5 zeolites and Fe-doped SBA-15 materials [46–49]. It has been observed that the maximum of the absorption band is shifted by the polymerization of the iron species, from 200 to 300 nm for Fe^{3+} isolated cations, to 300–400 nm for iron oxides clusters, and to more than 400 nm for large iron oxide nanoparticles. Here, the presence of a maximum at $\lambda = 245$ nm stands for the existence of isolated Fe^{3+} cations. However, since the absorption band is extended up to 350 nm, the presence of additional iron oxide clusters cannot be excluded.

To confirm these hypotheses, the catalytic materials were characterized by XPS. The high resolution O_{1s} and Fe_{2p} XPS spectra are given in Fig. 6. For comparison, the spectra of the bare γ-Fe_2O_3 NPs are also provided. In the O_{1s} region (see Fig. 6, A), the nanocomposite materials exhibit a broad band between 530.5 and 535.5 eV with a maximum at 532.5 eV, which can be ascribed to the O atoms of silica [50]. In addition, a small shoulder attributable to the O atoms coordinated to Fe, can be observed between 529.5 and 530.5 eV [51–53]. Our attempt to distinguish between the FeOFe and SiOFe species was unsuccessful, since the same degree of accuracy was obtained by fitting the data with two deconvolution curves (see Fig. 6, A) corresponding to the SiOSi and FeOFe species or with three deconvolution curves (not shown) corresponding to the SiOSi SiOFe and FeOFe species [50–55].

The analysis of the O_{1s} spectra cannot be further advanced since the shoulder corresponding to the Fe-coordinated O atoms is very weak, in comparison to the large band due to the silica O atoms. In addition, the O_{1s} spectrum of the bare γ-Fe_2O_3 NPs is rather complex. The

experimental spectra must be fitted by three curves with maxima at 529.7, 531.6 and 533 eV attributed to the FeOFe species, surface OH groups, and adsorbed water [51,52]. The two last peaks at large binding energies (BEs) are not distinguishable in the other spectra since they are overshadowed by the band due to silica.

In the Fe_{2p} core level (Fig. 6, B), two main bands can be observed at 710–712 eV and 724–726 eV which can be attributed, respectively, to the Fe $2p_{3/2}$ and Fe $2p_{1/2}$ electrons. Two satellite peaks of weak intensity at about 719 eV and 733 eV can be also observed. Concerning the bare γ-Fe_2O_3 NPs, the maxima for the $2p_{1/2}$ and $2p_{3/2}$ envelopes were found at 724.0 and 710.6 eV, which is in accordance with the previous studies [56,57]. For this sample, the high level of intensity obtained for the Fe_{2p} signal (about 10 times larger than the others), which implies a high signal-to-noise ratio, allowed us to fit the $2p_{3/2}$ envelope with a good accuracy using the multiplet energy data obtained for pure maghemite [57]. To the contrary, the sample corresponding to the undoped microporous solid (γ-Fe_2O_3/SiO_2 MS) was characterized by a very weak Fe_{2p} signal To explain that this sample, which contains more

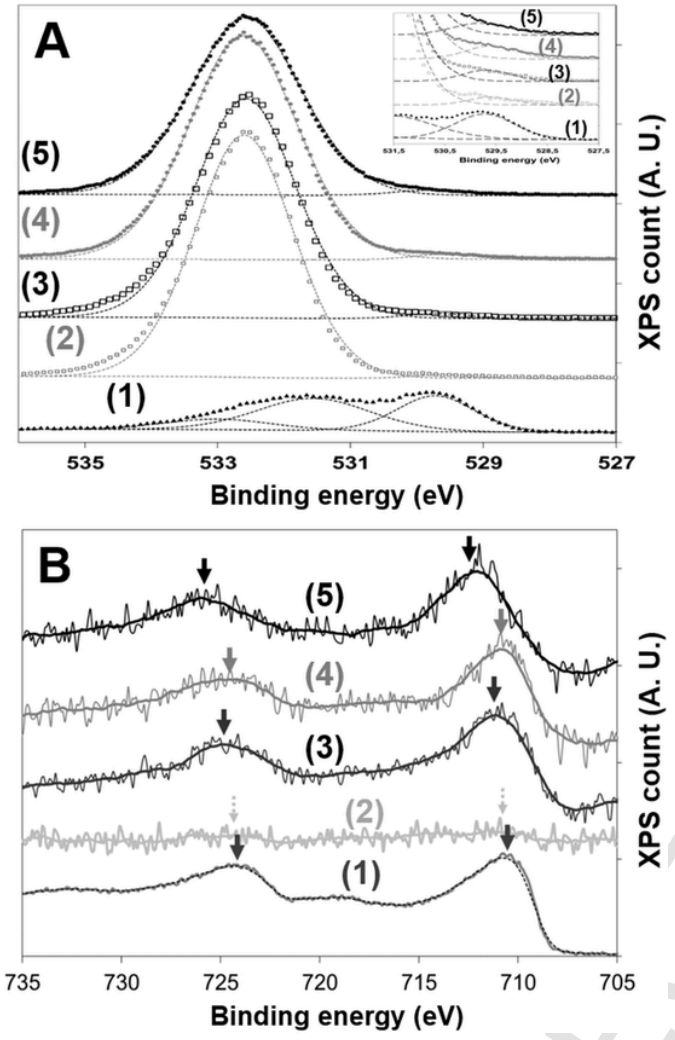

Fig. 6. High resolution XPS spectra of the catalysts. (A) O_{1s} region. The plots, the dashed lines, and the continuous lines correspond to the experimental data, the deconvolution curves obtained with a Gaussian-Lorentzian model, and the resulting fitting curve, respectively. In inset: enlargement for BEs between 531.5 and 527.5 eV. (B) Fe_{2p} region. The noisy lines and the superimposed continuous lines correspond to the raw data and the smoothed spectra, respectively. The arrows correspond to the maxima of the $2p_{3/2}$ and $2p_{1/2}$ peaks. All the Fe_{2p} spectra were normalized with respect to the $2p_{3/2}$ peak, except that of the γ-Fe_2O_3/SiO_2 MS sample, because of its too low signal. In all the pictures: (1): bare γ-Fe_2O_3 NPs; (2): γ-Fe_2O_3/SiO_2 MS; (3): Fe/γ-Fe_2O_3/SiO_2 MS; (4): γ-Fe_2O_3/SiO_2 *m*-MS; (5): Fe/γ-Fe_2O_3/SiO_2 *m*-MS.

than 8% in weight of Fe_2O_3, exhibits a nearly flat Fe_{2p} signal, it is necessary to consider that the material thickness analyzed by XPS is approximatively 10 nm. Since the γ-Fe_2O_3 NPs are well dispersed in the core of the microspheres, the amount of iron in the external shell analyzed by XPS is very low. For the three other nanocomposite materials, an intermediary and comparable intensity was found for the Fe_{2p} signal, which made possible to discuss about the nature of the iron species.

The larger intensity of the Fe_{2p} signal for the microporous doped material (Fe/γ-Fe_2O_3/SiO_2 MS) with respect to the undoped solid (γ-Fe_2O_3/SiO_2 MS) probably originates from the addition of $Fe(NO_3)_3$. The larger Fe_{2p} signal may reveal that the additional iron species are concentrated on the external shell of the microspheres. For this sample, the $2p_{1/2}$ and $2p_{3/2}$ bands are slightly shifted to larger BEs, in comparison to the pure γ-Fe_2O_3 NPs, respectively at 724.9 and 711.1 eV. This shift suggests that poorly crystallized Fe(III) oxo-hydroxide, analogous to ferrihydride (FeOOH) is formed, since it has been reported that for this phase the Fe $2p_{1/2}$ and Fe $2p_{3/2}$ bands are located at 711.5 eV and 725.0 eV [56,58]. An alternative explanation would be that the shift results from the interaction of isolated Fe^{3+} ions with silica, through the formation of Si–O–Fe bonds [53,59,60]. However, the isolated iron ions dispersed in silica are found at larger BEs, sometimes at more than 712 eV and 726 eV, because of the interaction of the iron atoms with the more electronegative silicon atoms [60]. Thus, for the Fe/γ-Fe_2O_3/SiO_2 MS sample, it is likely that the small shift noticed for the $2p_{3/2}$ and $2p_{1/2}$ peaks may result from the additional Fe^{3+} ions, consecutively to the formation of a poorly crystallized iron oxide phase.

As regards the undoped ordered mesoporous material (γ-Fe_2O_3/SiO_2 *m*-MS), the relatively large intensity of the Fe_{2p} signal can be explained by the fact that the γ-Fe_2O_3 NPs are aggregated, and that some of these aggregates are located not far from the external surface of the particles, as observed by TEM. The photoelectrons due to the NPs can therefore be emitted, and the Fe_{2p} signal is rather strong. Interestingly, this spectrum is identical to that of the bare NPs, which confirms that the Fe_{2p} signal results from the γ-Fe_2O_3 NPs. Finally, the doped ordered mesoporous material (Fe/γ-Fe_2O_3/SiO_2 *m*-MS) is characterized by maxima for the Fe $2p_{3/2}$ and Fe $2p_{1/2}$ envelopes at 711.9 and 725.6 eV, which indicates a shift of more than 1 eV in comparison to the undoped sample. Furthermore, owing to the composite nature of the Fe_{2p} signal in this material (both the γ-Fe_2O_3 NPs and the additional Fe^{3+} ions may contribute to the Fe_{2p} signal), it is likely that the Fe $2p_{3/2}$ and Fe $2p_{1/2}$ bands due to the additional iron species are found at larger BEs than these maxima. This strong difference in energy is indicative of the nature of the additional iron species. Only the isolated Fe^{3+} ions interacting with silica via Si–O–Fe bonds can be encountered at more than 712 eV and 726 eV [60]. Therefore, XPS confirms that for the Fe/γ-Fe_2O_3/SiO_2 *m*-MS sample, the doping iron is in the form of isolated Fe^{3+} ions (and/or small clusters of Fe^{3+} ions) dispersed in the silica framework.

3.2. Activity of the materials as heterogeneous Fenton catalysts

The performance of the nanocomposite materials as heterogeneous Fenton catalysts was evaluated by following the degradation of two model dyes (MO and RB5). The decolorization kinetics and TOC removal from the solutions were respectively obtained by UV–Vis spectroscopy, and measurement of the NPOC. The iron leaching of the catalysts was determined by analysis of the iron concentration in the supernatants after 4 h, using atomic absorption spectroscopy. Fig. 7 summarizes the results of these measurements for the four prepared catalysts.

As seen in Fig. 7, the catalytic activity for the degradation of MO and RB5 strongly depends on the structure of the catalytic materials. Whatever the model pollutant, the replacement of the microporosity by a regular mesoporosity and/or the Fe^{3+} doping leads to an increase of the decolorization rates, which is evidenced by an increase of both the initial rate (*v0*) and decolorization yields (*DY*) after 2 h. For MO, the effect of the porosity seems to be limited, since similar *DY* and *v0* were recorded (see Fig. 7A and B) with the two undoped materials (γ-Fe_2O_3/SiO_2 MS and γ-Fe_2O_3/SiO_2 *m*-MS). To the contrary, the degradation rate of MO is *greatly accelerated* by doping the silica framework with additional iron species. For the microporous solids, a moderate increase of *v0* and *DY* occurs, while a much stronger effect of the doping is observed with the mesoporosity. The best results are thus obtained for the Fe/γ-Fe2O3/SiO2 *m*-MS catalyst. This material allows a very fast and complete degradation of MO (DY = 99% at t = 25 min), with a value for *v0* 7 times larger than for the doped microporous catalyst (DY = 92% at t = 1 h) and 8 to 9 times larger than for the undoped materials (DY = 63% at t = 1 h). As for MO, a nearly total decolorization of the RB5 solutions (Fig. 7C and D) was achieved for all the catalysts, with the same order of efficiency. Slightly higher decolorization rates were obtained with RB5 (except for the γ-Fe_2O_3/SiO_2 MS catalyst, which exhibited a similar activity for both dyes). The far most active catalyst for RB5 was also the Fe/γ-Fe_2O_3/SiO_2 *m*-MS material. Interest-

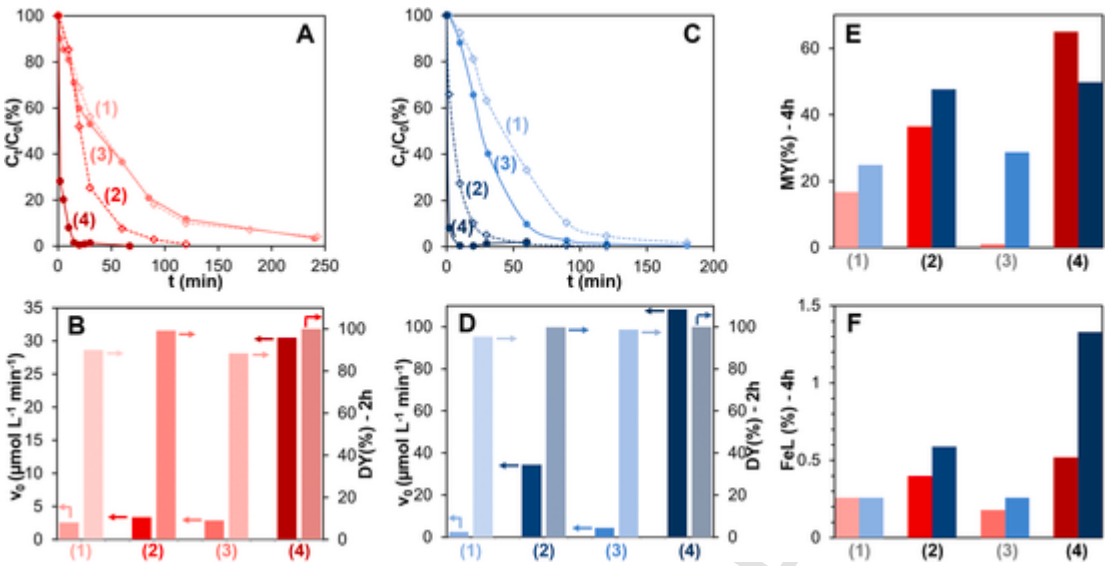

Fig. 7. Catalytic activity of the synthesized materials for the degradation of MO and RB5. (A): Kinetic curves for the decolorization of the MO solutions (The MO concentration, C_t is normalized to C_0, the MO concentration at t = 0). (B) Initial decolorization rates (v_0) and decolorization yields (*DY*) at 2 h for MO. (C) Kinetic curves for the decolorization of the RB5 solutions (The RB5 concentration, C_t is normalized to C_0, the RB5 concentration at t = 0). (D) Initial decolorization rates (v_0) and decolorization yields (*DY*) at 2 h for RB5. (E): Mineralization yields (*MY*) at t = 4 h for MO and RB5. (F): Percentage of leached iron (*FeL*) at t = 4h for MO and RB5. The numbers (1), (2), (3) and (4) respectively refer to the γ-Fe_2O_3/SiO_2 MS, Fe/γ-Fe_2O_3/SiO_2 MS, γ-Fe_2O_3/SiO_2 *m*-MS, and Fe/γ-Fe_2O_3/SiO_2 *m*-MS catalysts. The red and blue colours are respectively associated to MO and RB5. The arrows indicate the corresponding ordinate. (For interpretation of the references to color in this figure legend, the reader is referred to the Web version of this article.)

ingly, the mesoporous undoped material demonstrated a higher catalytic activity in the degradation of RB5 than its microporous counterpart. This difference with MO may be explained by the fact that RB5 is a much bigger dye, that makes it more difficult to access to the catalytic sites when they are located inside micropores. The mesoporous catalyst offers the advantage of larger pore diameters, which is of prime importance for such a big molecule.

In terms of TOC removal (Fig. 7, E), similar levels of mineralization were obtained for the two dyes. The mineralization of the solutions was globally slower than their decolorization, as it has been frequently mentioned in other published investigations [61–63]. The difference can be explained by the fact that the oxidation of the uncolored species resulting from the primary oxidation of the dyes proceeds very slowly. In particular, small carboxylic acids are formed at the end of the degradation process, which have been observed to be poorly sensitive towards oxidation [17,35]. However, a good correlation between the mineralization yields and the decolorizations rates was observed. As expected, the best mineralization yields at 4h were obtained for the **Fe**/γ-Fe_2O_3/SiO_2 *m*-MS catalyst (*MY* = 65% and 50% for MO and RB5, respectively). Slightly lower activities were noticed for the **Fe**/γ-Fe_2O_3/SiO_2 MS catalyst (*MY* = 36% and 48% for MO and RB5, respectively), while the two undoped solids were found to be poorly active for TOC removal (*MY* = 1–30%). It is also important to note that, because of the slow rate of the mineralization process, larger *MY* can be achieved after 24 h of reaction. For the most active catalyst, *MY* at 24 h is 66% and 84% for MO and RB5, respectively. The overall mineralization kinetics of the MO solutions for each catalyst can be found in Fig. S4.

The stability of the catalyst is a very important factor for practical applications. Indeed, the catalytic activity could be rapidly hindered by several factors including a continuous loss of the iron species from the surface, or changes in the porous structure and morphology during stirring. The iron leaching in the solutions was evaluated by measuring the percentage of dissolved iron after 4 h of reaction (*FeL*) for the both dyes. The results (Fig. 7, F) indicate that all the catalysts present a low level of leaching, in the same range as reported in other works for iron-containing mesoporous silica catalysts [21,48,62]. Interestingly, the doped materials present a slightly larger level of dissolved Fe, demonstrating that the species resulting from the addition of $Fe(NO_3)_3$ are more sensitive to leaching than the γ Fe_2O_3 NPs. Furthermore, the doped mesoporous catalyst has a larger leaching rate than its microporous counterpart, especially for the RB5 dye (1.3% of iron leached). This points out that the isolated Fe(III) species contained in the mesoporous solid are more sensitive to leaching than the more condensed iron oxide species contained in the microporous solid. Moreover, the larger values of *FeL* obtained with RB5 is indicative of the role played by the dye in the leaching process. It may be possible that the RB5 oxidation leads to the formation of intermediates that could enhance the dissolution of the Fe^{3+}/Fe^{2+} surface ions, by way of complexation or reduction reactions, as it has been evidenced for the Fenton degradation of phenolic compounds [64,65]. Regarding the evolution of the porosity and morphology, the catalysts were characterized by SEM and N_2 physisorption after Fenton reaction with MO. The results can be found in Figs. S5 and S6 and in Table S3. The SEM images (Fig. S5) reveal that the catalyst morphology is not altered, although the images display a small proportion of broken microspheres. This is especially observed for the mesoporous samples, which are probably more brittle, because of their hollow structure. The N_2 isotherms (Fig. S6 and Table S3) show that the porosity is maintained for all the catalysts, although a slight decrease is generally observed for the BET surface area and pore volume. This evolution may be explained by the adsorption of degradation compounds inside the pores [20], and/or by a moderate evolution of the silica framework during the catalytic test.

In order to further explore the catalytic behavior of the most active sample (Fe/γ-Fe_2O_3/SiO_2 *m*-MS) its activity was compared to that of the previously studied undoped microporous catalyst (γ-Fe_2O_3/SiO_2 MS) [20], in a large range of experimental conditions, using MO as model pollutant. Special attention was focused on the effects of pH, hydrogen peroxide concentration, amount of catalyst, and reusability tests. The obtained results are displayed in Fig. S7. To summarize, the Fe/γ-Fe_2O_3/SiO_2 *m*-MS material exhibits a much larger catalytic activity than the γ-Fe_2O_3/SiO_2 MS material whatever the situation (pH = 3 to 8, $[H_2O_2]_0$ = 6.8 × 10^{-3} to 0.68 mol L^{-1}, equivalent iron concentration $[Fe]_T$ = 1.6 × 10^{-3} to 3.15 × 10^{-2} mol L^{-1}). Furthermore, this catalyst is still active in very unfavorable conditions, for which the activity

of the conventional catalyst is negligible, such as at low amount, low H_2O_2 concentration, or for a slightly basic pH (Fig. S7, A-C). Regarding the reusability tests (Figs. S7 and D), both catalysts retained a good activity during five consecutive tests, although a decrease in reaction rates can be noticed. For the γ-Fe_2O_3/SiO_2 MS catalyst, the decrease in catalytic activity have been attributed to the contamination of the surface by degradation compounds intermediates [20]. A stronger decrease is observed for the Fe/γ-Fe_2O_3/SiO_2 *m*-MS catalyst, which can be correlated to the higher lixiviation level obtained for this sample. However, the main important point to note is that this catalyst is still more efficient than the undoped microporous catalyst, even after five consecutive use. It should also be noted that for the most active material, the supernatant containing the leached iron (after 4h of reaction) was tested as homogenous Fenton catalyst for the degradation of MO. A much slower degradation rate was recorded, in comparison to the same reaction in presence of the heterogeneous catalyst. This suggests that the degradation of MO mainly proceeds by a heterogeneous process, although a homogeneous process, resulting from the leached iron, simultaneously occurs. To check the importance of the catalytic activity due to leached ions, we have tested the supernatants of the reaction medium after 1h and 4h for the doped mesoporous catalyst, and 4h for the undoped microporous catalyst, on the MO degradation in the usual conditions (same temperature, pH and concentration of H_2O_2). The results of these experiments can be found in Fig. S8. As can be seen, the proportion of MO oxidized in homogenous phase is significant. Nevertheless, the activity of the heterogenous catalysts cannot be reduced to a reaction originating from leached iron, as the reaction rates in presence of the heterogenous catalysts are faster. In particular, the high decolorization rate of MO recorded with the Fe/γ-Fe_2O_3/SiO_2 *m*-MS catalyst is mainly due to a heterogenous reaction, since the activity of the supernatant after 1h of reaction - when decolorization is already achieved in heterogenous conditions - is relatively low.

These results clearly demonstrate the interest in adding small Fe(III) species inside the silica microspheres, through the use of $Fe(NO_3)_3$, to obtain a highly efficient magnetically separable Fenton catalyst. Since these species account for only 33% of the total iron introduced in the solids (the rest originating from the γ-Fe_2O_3 NPs), the strong increase of the reaction rates proves their high level of activity. Several explanations can be given to explain this efficiency. First, the small size of the Fe(III) species, which appear as single ions, clusters or very small oxide nanoparticles favor their good dispersion. This strongly enhances the number of active Fe-atoms that can generate the $HO^{\bullet}$ radicals by reaction with H_2O_2, in comparison to the relatively large γ-Fe_2O_3 NPs, where only a small part of the iron atoms, located on their surface, are accessible and can react with H_2O_2. Furthermore, a second factor related to a larger intrinsic activity of the additional Fe(III) species may also play a role. Third, the much larger activities may also be favored by the large pore volumes of the microspheres which are beneficial for molecular diffusion, facilitating the transport of the reactants to the additional active sites [21,23]. This last effect might be of prime importance to explain the much larger activities recorded for the mesoporous solids, with respect to the microporous materials. However, in view of the XPS and UV–vis characterizations, the additional Fe(III) species for the mesoporous solid are in a more dispersed form than for the microporous solid. Therefore, for the Fe/γ-Fe_2O_3/SiO_2 *m*-MS material, it is difficult to estimate the respective contributions of the mesoporosity and iron doping to the enhancement of the catalytic activity.

4. Conclusion

In this study, we investigated the relationships between the structure of several γ-Fe_2O_3/SiO_2 magnetic catalysts and their efficiency in the treatment of aqueous organics dyes by a heterogeneous Fenton process. The synthesis conditions of the catalytic materials were tuned in such a way that we were able to study independently the influence of two parameters. First, by adding a second surfactant during the synthesis, it was possible to control the porous structure of the silica support. Secondly, some catalysts were doped with extra-Fe(III) species, thanks to the addition of $Fe(NO_3)_3$ during the synthesis, along with the γ-Fe_2O_3 nanoparticles. The materials were characterized through the use of different methods, including SEM, TEM, N_2 physisorption measurements, XRD, UV–vis spectroscopy, magnetometry and XPS, and their catalytic efficiency was finally evaluated in the Fenton oxidation and mineralization of two dyes, methyl orange (MO) and reactive black 5 (RB5).

The novelty of this work lies in several features. First, we were able to prepare and characterize some new catalytic materials with an original and complex structure, especially those which were synthesized in presence of a second surfactant and/or with additional Fe^{3+} ions. We demonstrated that the addition of a second surfactant induces the presence of large amount of ordered mesoporous network similar to that of SBA-15 silicas, together with the appearance of a hole at the centre of the silica spherical particles, and a high level of aggregation for the γ-Fe_2O_3 nanoparticles. In addition, we observed that for the ordered mesoporous material, the extra-Fe(III) species are dispersed in the silica framework as isolated ions or small clusters, while for the microporous sample they seems to be more condensed.

Our results also confirm that the porosity and dispersion of Fe species play a major role in the performance of silica-supported catalysts for heterogeneous dark Fenton processes. The mesoporosity of the support favors a rapid diffusion of the reactants and products, and allows a faster dye degradation, especially for the large RB5 molecule. The strong activity of the dispersed Fe (III) species is illustrated by the results obtained with the doped catalysts, particularly for the mesoporous support.

Therefore, we were able to prepare here a highly efficient heterogenous Fenton catalyst, as demonstrated by the high level of activity of the mesoporous doped catalyst in the decomposition of both dyes. In addition, this sample retained a superior catalytic efficiency, for a large range of conditions, including different H_2O_2 concentrations, initial pH, catalyst dosages and reuse cycles. Furthermore, the low iron leaching level, and the moderate evolution of porosity and morphology indicate that the heterogeneous phase is stable under the reaction conditions. These interesting features are reinforced by the high magnetic susceptibility of the catalytic materials, which can be easily separated from the effluent by the use of a magnet or electromagnet. Thus, the combination of Fe^{3+} doping and addition of mesoporosity appears as a promising way to obtain highly efficient heterogeneous magnetic Fenton catalysts for wastewater treatment. Our future work will be to understand the role played by each iron species in the catalytic performances, by varying the amounts of γ-Fe_2O_3 nanoparticles and of additional Fe^{3+} ions. It will be also necessary to better identify the Fe species dispersed in silica, which requires the use of additional characterizations such as Mössbauer spectroscopy.

Declaration of competing interest

The authors declare that they have no known competing financial interests or personal relationships that could have appeared to influence the work reported in this paper.

Acknowledgments

We are very grateful to Delphine Talbot, Aude Michel, David Montero, Emmanuel Briot, Christophe Methivier, Christophe Callers, Emmanuel Aubry for their technical support, and Agnes Bée for the fruitful discussions. We equally acknowledge the scientific cooperation research program PROFAS between France and Algeria for the financial support.

Appendix A. Supplementary data

Supplementary data to this article can be found online at https://doi.org/10.1016/j.micromeso.2021.111373.

Funding

This research did not receive any specific grant from funding agencies in the public, commercial, or not-for-profit sectors.

Author statement

The authors declare that they have seen and approved the final version of the manuscript being submitted. They warrant that the article is the authors' original work, hasn't received prior publication and isn't under consideration for publication elsewhere.

References

[1] J.A. Dumesic, G.W. Huber, M. Boudart, Principles of heterogeneous catalysis, Handbook of Heterogenous Catalysis - Part 1 (Introduction), Wiley-VCH Verlag, Weinheim, 2008.
[2] D. Astruc, F. Lu, J. Ruiz Aranzaes, Angew. Chem. Int. Ed. 44 (2005) 7852–7872.
[3] L. Liu, A. Corma, Chem. Rev. 118 (2018) 4981–5079.
[4] M.A. Oturan, J.J. Aaron, Crit. Rev. Environ. Sci. Technol. 44 (2014) 2577–2641.
[5] E. Neyens, J. Baeyens, J. Hazard Mater. 98 (2003) 33–50.
[6] M.M. Bello, A.A.A. Raman, A. Asghar, Process Saf. Environ. Protect. 126 (2019) 119–140.
[7] M. Hartmann, S. Kullmann, H. Keller, J. Mater. Chem. 20 (2010) 9002–9017.
[8] S. Navalon, M. Alvaro, H. Garcia, silicas, zeolites, Appl. Catal., B 99 (2010) 1–26.
[9] S. Navalon, A. Dhakshinamoorthy, M. Alvaro, H. Garcia, ChemSusChem 4 (2011) 1712–1730.
[10] S.R. Pouran, A.A.A. Raman, W.M.A.W. Daud, J. Clean. Prod. 64 (2014) 24–35.
[11] M. Munoz, Z.M. de Pedro, J.A. Casas, J.J. Rodriguez, Appl. Catal., B 176–177 (2015) 249–265.
[12] T. Valdés-Solís, P. Valle-Vignón, M. Sevilla, A.B. Fuertes, J. Catal. 251 (2007) 239–243.
[13] X. Hu, B. Liu, Y. Deng, H. Chen, S. Luo, C. Sun, P. Yang, S. Yang, Appl. Catal., B 107 (2011) 274–283.
[14] K. Wang, H. Niu, J. Chen, J. Song, C. Mao, S. Zhang, Y. Gao, Appl. Surf. Sci. 404 (2017) 138–145.
[15] X. Tang, J. Huang, K. Liu, Q. Feng, Z. Li, M. Ao, Surf. Coating. Technol. 354 (2018) 18–27.
[16] R. Zhu, Y. Zhu, H. Xian, L. Yan, H. Fu, G. Zhu, Y. Xi, J. Zhu, H. He, Appl. Catal., B 270 (2020) 118891.
[17] C. Pulgarin, P. Peringer, P. Albers, J. Kiwi, J. Mol. Catal. 95 (1995) 61–74.
[18] N. Crowther, F. Larachi, Appl. Catal., B 46 (2003) 293–305.
[19] T. Valdés-Solís, P. Valle-Vignón, S. Álvarez, G. Marbán, A.B. Fuertes, Catal. Commun. 8 (2007) 2037–2042.
[20] N. Ferroudj, J. Nzimoto, A. Davidson, D. Talbot, E. Briot, V. Dupuis, A. Bee, M.S. Medjram, S. Abramson, Appl. Catal., B 136– 137 136– 137 (2013) 9–18.
[21] F. Martinez, G. Calleja, J.A. Melero, R. Molina, Appl. Catal., B 70 (2007) 452–460.
[22] K. Li, Y. Zhao, C. Song, X. Guo, Appl. Surf. Sci. 425 (2017) 526–534.
[23] S. Amelia, W.B. Sediawan, I. Prasetyo, M. Munoz, T. Ariyanto, J. Environ. Chem. Eng. 8 (2020) 102921.
[24] M. Xia, C. Chen, M. Long, C. Chen, W. Cai, B. Zhou, Microporous Mesoporous Mater. 145 (2011) 217–223.
[25] M. Xia, M. Long, Y. Yang, C. Chen, W. Cai, B. Zhou, Appl. Catal., B 110 (2011) 118–125.
[26] Y. Ling, M. Long, P. Hu, Y. Chen, J. Huang, J. Hazard Mater. 264 (2014) 195–202.
[27] H. Lim, J. Lee, S. Jin, J. Kim, J. Yoon, T. Hyeon, Chem. Commun. (2006) 463–465.
[28] J.A. Melero, G. Calleja, F. Martínez, R. Molina, Catal. Commun. 7 (2006) 478–483.
[29] R. Zhang, H. You, D.H. Wu, Desalin. Water Treat. 57 (2015) 12010–12018.
[30] S. Karthikeyan, M.P. Pachamuthu, M.A. Isaacs, S. Kumar, A.F. Lee, G. Sekaran, Appl. Catal., B 199 (2016) 323–330.
[31] Z. Wan, J. Wang, J. Hazard Mater. 324 (B) (2017) 653–664.
[32] G. Zhan, H.C. Zeng, Chem. Mater. 28 (2016) 4572–4582.
[33] Z. Chen, Y. Liang, J. Hao, Z.M. Cu, Langmuir 32 (2016) 12774–12780.
[34] N. Ferroudj, D. Talbot, A. Michel, A. Davidson, S. Abramson, J. Photochem. Photobiol., A 338 (2017) 85–95.
[35] M. Cohen, N. Ferroudj, A. Combes, V. Pichon, S. Abramson, J. Environ. Chem. Eng. 7 (2019) 102987.
[36] C. Farrell, F. Hassard, B. Jefferson, T. Leziart, A. Nocker, P. Jarvis, Sci. Total Environ. 624 (2018) 638–647.
[37] R. Massart, IEEE Trans. Magn. 17 (1981) 1247–1248.
[38] V. Cabuil, Ferrofluides à base de maghémite : synthèse, propriétés physicochimiques et magnéto-optiques, Ph.D. thesis, Université Pierre et Marie Curie, Paris, 1987.
[39] N. Andersson, R.W. Corkery, P.C.A. Alberius, J. Mater. Chem. 17 (2007) 2700–2705.
[40] L. Xiang, S. Royer, H. Zhang, J.-M. Tatibouët, J. Barrault, S. Valange, J. Hazard Mater. 172 (2009) 1175–1184.
[41] J.S. Beck, J.C. Vartulli, W.J. Roth, M.E. Leonowicz, C.T. Kresge, K.D. Schmitt, C.T.-W. Chu, D.H. Olson, E.W. Sheppard, S.B. Mac Cullen, J.B. Higgins, J.L. Schlenker, J. Am. Chem. Soc. 114 (1992) 10834–10843.
[42] D.Y. Zhao, J.L. Feng, Q.S. Huo, N. Melosh, G.H. Fredrickson, B.F. Chmelka, G.D. Stucky, Science 279 (1998) 548–552.
[43] A. Galarneau, M. Nader, F. Guenneau, F. Di Renzo, A. Gedeon, J. Phys. Chem. C 111 (2007) 8268–8277.
[44] A. Sayari, B.-H. Han, Y. Yang, J. Am. Chem. Soc. 126 (2004) 14348–14349.
[45] J. Torrent, V. Barron, Diffuse reflectance spectroscopy of iron oxides, in: A.T. Hubbard (Ed.), Encyclopedia of Surface and Colloid Science, Marcel Dekker, New-York, 2002, pp. 1438–1446.
[46] J. Pérez-Ramírez, J.C. Groen, A. Brückner, M.S. Kumar, U. Bentrup, M.N. Debbagh, L.A. Villaescusa, J. Catal. 232 (2005) 318–334.
[47] F. Zhang, X. Chen, J. Zhuang, Q. Xiao, Y. Zhong, W. Zhu, Catal. Sci. Technol. 1 (2011) 1250–1255.
[48] C. Cornu, J.L. Bonardet, S. Casale, A. Davidson, S. Abramson, G. André, F. Porchet, I. Grcic, V.T.D. Vujevic, N. Koprivanac, J. Phys. Chem. C 116 (2012) 3437–3448.
[49] L. Li, Q. Meng, J. Wen, J. Wang, G. Tu, C. Xu, F. Zhang, Y. Zhong, W. Zhu, Q. Xiao, Microporous Mesoporous Mater. 227 (2016) 252–257.
[50] J. Serra, P. Gonzalez, S. Liste, C. Serra, S. Chiussi, B. Leon, M. Perez-Amor, H.O. Ylanen, M. Hupa, J. Non-Cryst. Solids 332 (2003) 20–27.
[51] A. Glisenti, J. Chem. Soc., Faraday Trans. 94 (1998) 3671–3676.
[52] M. Aronniemi, J. Sainio, J. Lahtinen, Appl. Surf. Sci. 253 (2007) 9476–9482.
[53] X. Liang, R. Yang, G. Li, C. Hu, Microporous Mesoporous Mater. 182 (2013) 62–72.
[54] V.P. Zakaznova-Herzog, H.W. Nesbitt, G.M. Bancroft, J.S. Tse, Surf. Sci. 600 (2006) 3175–3186.
[55] R. Włodarczyk, J. Sauer, X. Yu, J.A. Boscoboinik, B. Yang, S. Shaikhutdinov, H.-J. Feund, J. Am. Chem. Soc. 135 (2013) 19222–19228.
[56] R.M. Cornell, U. Schwertmann, The Iron Oxides: Structure, Properties, Reactions, Occurrences and Uses, Wiley-VCH Verlag, Weinheim, 2003.
[57] A.P. Grosvenor, B.A. Kobe, M.C. Biesinger, N.S. McIntyre, Surf. Interface Anal. 36 (2004) 1564–1574.
[58] R. Barik, B. Kumar Jena, A. Dash, M. Mohapatra, RSC Adv. 4 (2014) 18827–18834.
[59] C.-T. Wang, S.-H. Ro, Appl. Catal., A 285 (2005) 196–204.
[60] A. De Stephanis, S. Kaciulis, L. Pandolfi, Microporous Mesoporous Mater. 99 (2007) 140–148.
[61] I. Mazilu, C. Ciotonea, A. Chirieac, B. Dragoi, C. Catrinescu, A. Ungureanu, S. Petit, S. Royer, E. Dumitriu, Microporous Mesoporous Mater. 241 (2017) 326–337.
[62] F. Martínez, R. Molina, M.I. Pariente, J.A. Siles, J.A. Melero, Catal. Today 280 (2017) 176–183.
[63] L.M. Pastrana-Martínez, N. Pereira, R.A. Lima, J.L. Faria, H.T. Gomes, A.M.T. Silva, Chem. Eng. J. 261 (2015) 45–52.
[64] C.P. Huang, Y.-H. Huang, Appl. Catal., A 346 (2008) 140–148.
[65] G.B. Ortiz de la Plata, O.M. Alfano, A.E. Cassano, Appl. Catal., B 95 (2010) 1–13.